



Opto-electro-mechanical percolative composites from 2D layered materials: Properties and applications in strain sensing

Sangram Mazumder^{a,1}, Jorge A. Catalan^{b,1}, Alberto Delgado^{b,1}, Hisato Yamaguchi^c,
Claudia Narvaez Villarrubia^c, Aditya D. Mohite^{c,d}, Anupama B. Kaul^{a,e,*}

^a Department of Materials Science and Engineering; PACCAR Technology Institute, University of North Texas, Denton, TX, 76203, USA

^b Department of Metallurgical, Materials and Biomedical Engineering, University of Texas at El Paso, El Paso, TX, 79968, USA

^c Los Alamos National Laboratory, MPA-11 Materials Synthesis & Integrated Devices, Materials Physics and Applications Division, P.O. Box 1663, Los Alamos, NM, 87545, USA

^d Chemical and Biomolecular Engineering, Rice University, Houston, TX, 77251, USA

^e Department of Electrical Engineering, University of North Texas, Denton, TX, 76203, USA

ARTICLE INFO

Keywords:

2D materials
Solution exfoliation
MoS₂
Graphene
WS₂
Strain sensors
Composites
Optical absorption

ABSTRACT

The fragmentation rate (*FR*) of two-dimensional layered materials (2DLMs) MoS₂, WS₂, and graphene in *N*-methyl-pyrrolidinone (NMP) was computed, where *FR* is a measure of the particle size reduction with ultrasonication time. For the 2DLMs, the highest *FR* generally occurred for sonication times $t_{sonic} = 30$ min, with $FR_{Graphite} \sim -1176.4 \mu\text{m}\cdot\text{hr}^{-1}$, $FR_{WS2} \sim -32.4 \mu\text{m}\cdot\text{hr}^{-1}$ and $FR_{MoS2} \sim -3.8 \mu\text{m}\cdot\text{hr}^{-1}$. This is in contrast to a non-layered material, Al nanoparticles, where $FR_{Al} \sim 0 \mu\text{m}\cdot\text{hr}^{-1}$ for $t_{sonic} = 30$ min. Knowledge of the particle size as a function of t_{sonic} has not been reported previously for 2DLMs, and is extremely important as these materials are integrated into additively manufactured platforms, such as ink-jet printing and three-dimensional (3D) printing. The treated materials were then infused with two types of polymers, flexible and stretchable polyisoprene, and an optically transparent acrylic, poly-methyl-methacrylate (PMMA) for opto-electro-mechanical strain-based sensing device applications. In particular, the hybrid composites of graphene with optically transparent and bendable PMMA revealed the potential of forming opto-mechanical filters, where optical filtering can be engineered through the graphene loading. The polyisoprene-graphene composites were piezo-resistive with potential for wearable electronics, where mechanical strain, as induced at joint movements on a finger for example, modulates the current with joint displacement. Strain levels of up to 200% were observed and the gauge factor of these devices was measured to be ~ 75 which is $> 10\times$ higher compared to conventional metal-foil based strain sensors. This work sheds fundamental insights into the role of sonication on the materials properties of 2DLMs in solution dispersions and shows their potential in hybrid composites for opto-electro-mechanical strain based sensing applications and in wearable electronics.

1. Introduction

Since the mechanical exfoliation of graphene from parent graphite in 2004 [1], fascinating properties of this remarkable material have been unveiled [2], which have led to insights into its exceptional flexibility, mechanical strength, high electrical conductivity and transparency. The surge in applications arising from graphene cover topics ranging from its use in transparent conducting electrodes for replacing indium tin oxide (ITO), displays and touch screens, solar cells, ultra-capacitors, chemical sensors, and nanoelectronics [3–9] Just like graphene [10], the broader class of two dimensional layered materials

(2DLMs), such as hexagonal boron nitride (h-BN), transition metal dichalcogenides (TMDCs), transition metal oxides and tertiary compounds of carbo-nitrides, possess equally intriguing properties [11,12]. Amongst the TMDCs, several materials are semiconducting with an inherent band gap in contrast to graphene [9]. In certain cases, these materials turn from indirect band gap semiconductors for bulk crystals, to direct band gap as dimensionality is reduced to monolayers. The TMDCs have the general formula MX₂ with M being a transition metal (commonly, but not limited to, Mo, W, Nb, Ta, Ti), and X is a chalcogen (S, Se, Te). While the bulk crystals of several TMDCs have been explored since the 60's [11], it was not until recently that renewed

* Corresponding author. Department of Materials Science and Engineering; PACCAR Technology Institute, University of North Texas, Denton, TX, 76203, USA.
E-mail address: anupama.kaul@unt.edu (A.B. Kaul).

¹ These authors contributed equally to the work.

interest in TMDCs has surfaced again, given that their 2D analogues are now routinely isolated, leveraging advances made largely on graphene research.

With the *intra-layer* bonding in graphene and TMDCs being through the strong covalent interaction, the *inter-layer* bonding however is via the weak van der Waals interaction. It is precisely this weak inter-layer interaction that has rendered the success of scotch-tape assisted mechanical exfoliation, where individual layers are peeled to yield monolayer and few layer molecular membranes from the bulk crystal for materials analysis and device integration. At the same time, large-area and scalable production techniques of these materials are vitally necessary for insertion into practical applications. In this regard, top-down solution-based exfoliation in organic solvents is gaining increasing attention currently, which has yielded mono and few layer nanosheets [13–16]. Despite the fact that these solution based approaches may lead to more structural imperfections compared to vapor-based techniques, the 2DLMs nonetheless appear to be adequate for flexible electronics, catalysis and composite materials applications, where material quality and defect-density requirements are less stringent compared to high-frequency, low-power digital electronics for example [7].

For solution-based production, Coleman et al. [14–16] and others [17–19], have studied the role of solvent chemistries such as cyclohexanone, N-methyl-pyrrolidinone (NMP), di-methyl-formamide (DMF), 2-propanol (IPA) and di-methyl-acetamide (DMA) on the exfoliation efficacy of 2DLMs using ultrasonication. Here ultrasonication jets created in the chemically active solvents, mechanically shear the crystal planes to overcome the weak inter-layer van der Waals bonding in the bulk crystals to yield nanomembranes in the dispersions.

Given the increasing importance of solution-based exfoliation and its imminent potential for translational applications, in this paper we have conducted a detailed analysis of the effect of ultrasonication on the structural characteristics of TMDCs, in particular MoS₂ and WS₂ as well as graphite, from which a fragmentation rate *FR* was computed for the first time for these materials, and contrasted with a non-layered material, Al nanoparticles for comparative analysis. This has shed fascinating insights into the structural attributes of 2DLMs and their synergistic effects with chemical exfoliants in solution. The solvent used in our study was NMP, a commonly used organic solvent for exfoliating a range of 2DLMs. Knowledge of the particle size variation, which was measured using a dynamic light scattering technique (described in “Experimental Section”), with ultrasonication time has not been reported previously, and is particularly important for applications such as ink-jet printing, 3D printing, and other additive manufacturing techniques, in addition to composite-based applications of 2DLMs. Besides particle size analysis, other characterization techniques were also implemented here in parallel, which included scanning electron microscopy (SEM), Raman Spectroscopy and X-ray diffraction (XRD), to correlate the *FR* data to particle size distribution, deduce layer number, and analyze the nature of the induced stresses in the nanomembranes due to ultrasonication, respectively.

Once the *FR* data was computed for the 2DLMs as a function of sonication time, the dispersions were then infused with polymeric materials to yield composites. Composites offer a facile means to tailor the properties of hybrid, dissimilar material systems for applications ranging from optoelectronics to strain sensors. Ruoff et al. [20] and others [21] have conducted early work on composites of graphene and graphene-like materials. In our work, hybrid composites of 2DLMs were formed with lightweight stretchable elastomers, as well as cross-linked, optically transparent acrylics for the realization of opto-electro-mechanical strain-based sensors. Interestingly, some of these 2DLMs intrinsically exhibit unique strain-induced effects, where the optical band gap was found to decrease for monolayer and bilayer MoS₂ [22]. Molybdenum disulfide also has the ability to accommodate strains well up to 11% without showing signs of mechanical degradation, while a strain-induced direct-to-indirect band gap transition for monolayer

MoS₂ has also been observed through photoluminescence measurements [22]. Interestingly, MoS₂ has been integrated with PMMA previously for optical limiting applications [23].

While composites of all of the four solution dispersed materials were formed in both elastomers and acrylics, here we have successfully shown the modulation of the strain-induced optical and electrical properties of the graphene-based polyisoprene and PMMA composites. Given the mechanical and electrical properties of graphene, it makes graphene a perfect candidate for strain based opto-electro-mechanical sensors. Flexible, stretchable and strain-based sensors have long been desirable for wearable electronics and life monitoring systems [24–29]. In strain sensors, external forces acting on the material cause geometrical and/or mechanical deformations, which are then transduced and detected as an optical and/or an electrical signal [25–28]. In our PMMA-graphene composites we have measured the optical absorbance and electrical resistance change as a function of strain (in bending mode) and graphene loading. Similarly, studies were also conducted with the graphene-polyisoprene composites, where electrical resistance was measured as a function of tensile strain and graphene loading, and this piezoresistive response was explained on the basis of percolation theory and tunneling mechanisms occurring within the composites. We have demonstrated this graphene-polyisoprene sensor for utility in practical applications, specifically for detecting bodily motion when it was attached to a finger and the resistance was modulated with joint movement. Our strain-based sensor exhibited good linearity with minimal hysteresis, and strain levels and gauge factors of up to 200% and 75, respectively, were measured. The measured gauge factors are > 10X larger compared to conventional metal-foil based strain sensors [30,31], and appear to be attractive for personal health monitoring, rehabilitation and wearable electronics. In 2018, Song et al., [32] developed a skin mountable sensor with tunable stretchability and a gauge factor ranging from 7.2 to 474.8, where tiny facial movements were detected to infer emotions. The strain sensors fabricated in this work have a gauge factor within the above mentioned range and from this we infer there is a strong likelihood that our sensors may also be adapted to detect tiny movements for various future studies, besides detecting larger scale body movements such as that associated with finger movements demonstrated here.

2. Results and discussion

2.1. Structural characterization of the dispersions

Bulk powders of MoS₂, WS₂, graphite and Al were immersed in NMP at sonication times ranging from 0.5, 6, 12 and 18 h, while the ultrasonication power was fixed. For each of the four material dispersions, the first of five samples was the control, i.e. the bulk, *as received* powder, while the remaining four samples were each subject to the four sonication times mentioned. The sonicated materials were then transferred to an IPA solution in preparation for the particle size measurement, which was conducted using the MicroTac (see “Experimental Section”). The MicroTac utilizes dynamic light scattering (DLS) to determine the particle size of dispersed species using three lasers, two blue lasers at wavelengths λ in the range of 360–480 nm, and one red laser at λ in the range of 625–700 nm. Subsequently, the dispersions were placed onto Si and SiO₂ (oxide thickness \sim 270 nm) substrates, in order to analyze them using SEM, Raman Spectroscopy, and XRD, as appropriate.

2.1.1. Molybdenum disulfide (MoS₂)

The particles in the *as-received* MoS₂ powder or control were measured to have a mean particle size $S_{MoS_2} \sim 6.5 \mu\text{m}$, which was fit to a Nagakami probability distribution (see supplementary section). After subjecting the MoS₂ to ultrasonication, the S_{MoS_2} shifted to the left as t_{sonic} increased, as shown by the data in Fig. 1a, where S_{MoS_2} ($t_{sonic} = 30 \text{ min}$) $\sim 4.5 \mu\text{m}$. As sonication proceeded, multi-modal

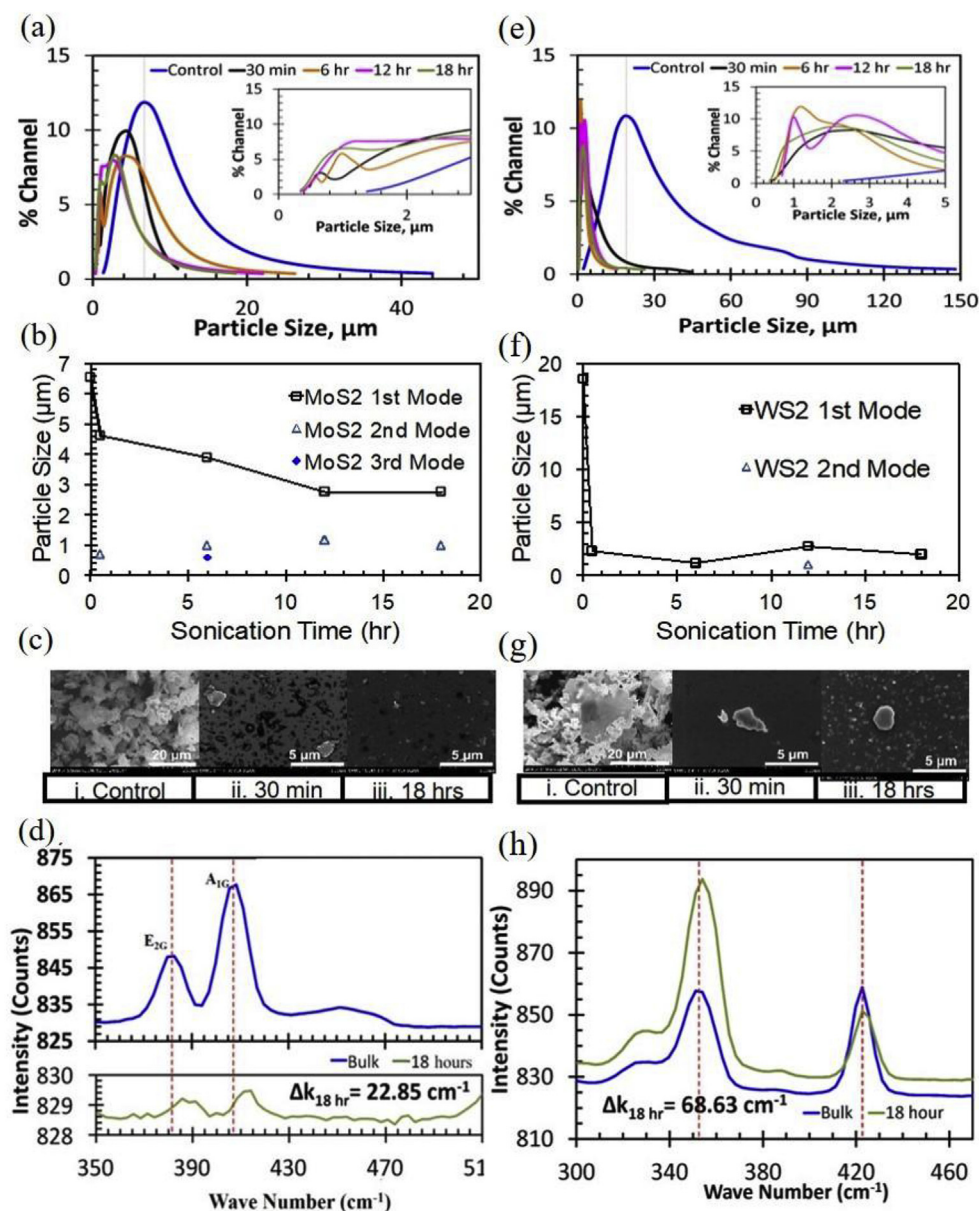


Fig. 1. Structural characterization of treated MoS₂ shown in (a)–(d) while (e)–(h) refer to WS₂. a) particle size distribution measured using the MicroTac for $t_{sonic} = 0$ min (control), 30 min, 6 h, 12 h and 18 h; inset shows the peaks in the MoS₂ distribution at lower length scales. b) Mean particle size S as a function of t_{sonic} showing the 1st, 2nd and 3rd modes in the distribution function. c) SEM micrographs showing a higher population of smaller particles in the background for samples where $t_{sonic} = 18$ h (iii) compared to the control (i). d) Raman shift $\Delta k \sim 22.85 \text{ cm}^{-1}$ for MoS₂ is indicative of 2–3 layer thick platelets where $t_{sonic} = 18$ h compared to the control. Spatial resolution of Raman system was $\sim 1 \mu\text{m}$. Characterization of treated WS₂ in (e)–(h). e) particle size distribution showing $S_{WS_2} \sim 18.5 \mu\text{m}$ for *as received* material and the inset shows the WS₂ particles over smaller length scales. f) S as a function of t_{sonic} showing the 2nd mode occurring at $t_{sonic} = 12$ h. g) WS₂ SEM micrographs showing a higher population of smaller particles in the background for the longer $t_{sonic} = 18$ h in (iii) compared to the control in (i). h) Raman shift $\Delta k \sim 68.63 \text{ cm}^{-1}$ is indicative of few layer (~ 3 layers)^[32] WS₂ for samples where $t_{sonic} = 18$ h.

distributions were observed, such as bi-modal (2nd mode) and tri-modal (3rd mode), that are illustrated in the magnified plot in the inset of Fig. 1a. Fig. 1b provides a quantitative measure of the 1st, 2nd, and 3rd modes as they appear for MoS₂ with increasing t_{sonic} . In the case of MoS₂, a bimodal distribution was observed for all t_{sonic} considered up to 18 h, while a trimodal distribution was evident at $t_{sonic} = 6$ h, that later evolved into a bimodal for $t_{sonic} = 12$ h. This suggests that as the powder is ultra-sonicated for a longer duration at the same power level, the tri-modal population evolves toward a bi-modal distribution with a net reduction in S_{MoS_2} . The origin for the higher-order modes comes about due to a transition from the “coarse” regime toward the “fine” particle regime. Once the fragmentation proceeds to completion as a function of time, migration toward a single mode distribution may arise, unless other sonication parameters, such as power or frequency are varied, which may provide an additional driving force for the propagation toward a lower S .

While S was measured quantitatively using DLS, we also conducted direct physical characterization of the dispersions using SEM, as shown by the images in Fig. 1c(i)–(iii). Here, we clearly see smaller particulates in the background on the Si substrate that were sonicated for 18 h

(Fig. 1c(iii)) when compared to the control sample, where $t_{sonic} = 0$ h (Fig. 1c(i)) that depicts much larger particles. Consequently, Raman Spectra (spatial resolution of the Raman system was $\sim 1 \mu\text{m}$) obtained for MoS₂ shown in Fig. 1d indicates a Raman Shift, $\Delta k = A_{1g} - E_{2g} = 22.8 \text{ cm}^{-1}$ for samples where $t_{sonic} = 18$ h, which is lower when compared to $\Delta k \sim 25 \text{ cm}^{-1}$ for bulk MoS₂ or the control. This Δk shift of $\sim 22.8 \text{ cm}^{-1}$ is indicative of 2–3 layer thick platelets of MoS₂ for samples where $t_{sonic} = 18$ h. Exfoliation of 2DLMs will also reduce the aspect ratio of the particles due to reduction in the lateral dimensions. Therefore, the Raman shift attributed to the reduction in layer number by exfoliation is also potentially due to changes in the lateral size. Prior work where similar sonication times were used confirmed the presence of exfoliated material with ~ 4 layers, although the initial concentration of MoS₂ was lower in their work [13,17].

2.1.2. Tungsten disulfide (WS₂)

Another sulfide TMDC, specifically WS₂, was analyzed to understand the impact of sonication on its structural and morphological character. The *as-received* WS₂ bulk powder exhibited $S_{WS_2} \sim 18.5 \mu\text{m}$, as shown by the data in Fig. 1e, where the Burr probability distribution

function appeared to provide a good fit (see supplementary section). As sonication proceeded, the peak in the distribution shifted toward the left. For example, $1.8 \mu\text{m} < S_{WS_2} (t_{sonic} = 30 \text{ min}) < 3.0 \mu\text{m}$ but for $t_{sonic} > 30 \text{ min}$ no further reduction in S_{WS_2} was noted up to $t_{sonic} = 18 \text{ h}$, as observed in Fig. 1f; this is unlike MoS_2 where a steady decrease in S_{MoS_2} was noted (Fig. 1b) as a function of t_{sonic} . A bimodal distribution for WS_2 was evident at $t_{sonic} = 12 \text{ h}$, as seen in Fig. 1e (inset) and Fig. 1f. The separation between the 1st and 2nd modes was small $\sim 2 \mu\text{m}$, and this 2nd mode vanished after $t_{sonic} = 18 \text{ h}$. This suggests that even though t_{sonic} increased, S_{WS_2} remained within the same range even for $t_{sonic} = 12 \text{ h}$ given the proximity of both modes at this sonication time.

The structural characteristics of WS_2 after sonication were analyzed using SEM, just as for MoS_2 , and the data are shown in Fig. 1g. The Raman shift for $t_{sonic} = 18 \text{ h}$ was computed to be $\Delta k_{18\text{hr}} = 68.63 \text{ cm}^{-1}$ as shown in Fig. 1h, suggesting that the number of layers in the sonicated samples is within a few layers (~ 3 layers) [33]. As previously illustrated by Rice et al. [34] a small shift in the A_{1g} peak to lower frequencies occurs for both monolayer and few-layer MoS_2 a function of induced strain. A comparatively larger shift was observed in the E_{2g}^1 mode for both monolayer (slightly higher at -2.1 cm^{-1} per % strain) and few-layer MoS_2 (lower at -1.7 cm^{-1} per % strain). Similar trends were also seen in graphene, where capped and uncapped samples of varying thickness were studied and the results suggest that the Raman shift may be correlated to strain also. Hence, the Raman shift observed in our study here may also be attributed to strain-induced phonon shifts in the 2D materials.

2.1.3. Graphene

For the *as received* graphite powder, S_{Graphite} was measured to be $\sim 837 \mu\text{m}$, and the Extreme Value probability distribution function provided a good fit to the data. Despite the fact that the particulates in the graphite powder were considerably coarser than the TMDCs, nonetheless, a shift to the left was seen in S_{Graphite} as t_{sonic} increased, where a reduction in particle size by $\sim 73\%$ was noted, i.e. $S_{\text{Graphite}} (t_{sonic} = 30 \text{ min}) \sim 296 \mu\text{m}$, as seen in Fig. 2a. From Fig. 2b and inset of Fig. 2a, a bimodal distribution is also evident for $t_{sonic} = 30 \text{ min}$ and 6 h , and after $t_{sonic} > 12 \text{ h}$, a single mode distribution arises where $S_{\text{Graphite}} (t_{sonic} > 12 \text{ h}) \sim 5.5 \mu\text{m}$. In Fig. 2c, SEM micrographs show the reduction in particle size with increasing sonication time (Fig. 2c-(ii)-(iii)) when compared to the bulk (Fig. 2c-(i)). The samples with $t_{sonic} = 18 \text{ h}$ exhibited an $S_{\text{Graphite}} \sim 3.89 \mu\text{m}$. Shown in Fig. 2d is the Raman spectra for graphite, where the well-defined D, G and 2D peaks occur at 1350 cm^{-1} , 1580 cm^{-1} and 2700 cm^{-1} , respectively. The D band is attributed to the in-plane A_{1g} zone-edge mode and can be used to monitor the defect distribution of graphite films by computing the D/G ratio [35]. As shown in Table 1, the D/G ratio was calculated to be 0.98 for samples where $t_{sonic} = 18 \text{ h}$, compared to the bulk, *as received* material where the ratio was 0.87, which suggests that the defect distribution in the sonicated graphene dispersions increased slightly, as expected by exposure to sonication. Fig. 2d also reveals that the Raman intensity ratio I_{2D}/I_G was < 2 which suggests that our dispersions comprise of multilayer graphene nanomembranes.

2.1.4. Aluminum

While 2DLMs show a variation of particle size with sonication time to varying degrees, we also characterized the structural changes arising in a non-layered material, Al nanoparticles as a function of t_{sonic} for comparative analysis. The *as received* Al powder showed $S_{Al} \sim 26.16 \mu\text{m}$, and was best fit to the Birnbaum Saunders distribution (see supplementary section). The $S_{Al} (t_{sonic} = 30 \text{ min}) \sim 26.16 \mu\text{m}$, which was same as the initial bulk value, as depicted in Fig. 2e. Moreover, a bimodal distribution was evident when $t_{sonic} = 6 \text{ h}$, but the Al particles were still coarse, unlike the rapid reduction noted in particle size for 2DLMs, i.e. MoS_2 , WS_2 and graphite within just 30 min of sonication. The morphological changes in the dispersions were not greatly altered

with sonication, as is evident from the SEM images in Fig. 2g-(i)-(iii). Here, the clear, spherical morphology of the Al nanoparticles is visible for all of the ultra-sonication times considered, which once again validates the unique structural characteristics of the 2DLMs that makes them well suited for chemical exfoliation using sonication.

2.1.5. Fragmentation rate (FR)

We now compare the quantitative outcomes of the fragmentation rate (FR). The FR is simply a measure of the particle size reduction with sonication time for all of the materials analyzed here up to a sonication time of 30 min, where the data are shown in Fig. 2h. For the 2DLMs, the greatest particle size reduction or the highest FR generally occurred within the initial 30 min, after which point the FR varied less sensitively with time. This is in contrast to the non-layered material, Al, where $FR \sim 0 \mu\text{m h}^{-1}$ for the first 30 min where no reduction in particle size was noted. The highest FR occurred for graphite powder where FR_{Graphite} was $\sim -1176.4 \mu\text{m-hr}^{-1}$, and the FR_{WS_2} and FR_{MoS_2} were determined to be $\sim -32.4 \mu\text{m-hr}^{-1}$ and $-3.8 \mu\text{m-hr}^{-1}$, respectively; here the WS_2 also incidentally had a similar initial particle size comparable to the Al powder. Despite the fact that the FR_{MoS_2} was the lowest, the Raman analysis however clearly indicated that the ensuing platelets were 2–3 layers thick, and suggested that the sonication conditions used were effective in shearing the bulk material into few layer crystallites. As mentioned, the FR_{Al} was $\sim 0 \mu\text{m-hr}^{-1}$, which corroborates the strong metallic and covalent bonds in Al and conventional bulk 3D materials that resist particle fragmentation, at least during the initial period of sonication, which is distinctly different to the shearing and fragmentation mechanisms evident in 2DLMs. Thus, the FR of 2D materials (graphene, MoS_2 and WS_2) are higher than the FR of the Al due to differences in the bonding mechanisms. This implies that sonication of 2D materials in common solvents allows effective particle size reduction, whereas for non-layered materials such as Al, it is not an efficient approach to reduce particle size.

2.1.6. X-ray diffraction

Given the high energy jets created within the liquids during sonication, it is not surprising that significant forces and compressive and/or tensile stresses are likely to be induced within the crystallites as sonication proceeds. The presence of stress modes in these sonicated materials was analyzed using XRD, which provides the $2-\theta$ shift in the XRD spectra that comes about as a result of changes in d -spacing in the crystal lattice for the four sonicated materials considered here. Shown in Fig. 3 is the XRD spectra obtained for MoS_2 , WS_2 , graphite and Al, at $t_{sonic} = 0 \text{ h}$ (control), 30 min, 6 h, 12 h, and 18 h. In general, strain in materials including semiconductors modifies lattice constant and crystal symmetry, causing the energy band to shift, which in turn induces changes in the relative effective masses. From the particle size measurements, the FR was the highest for the 2DLMs within the initial 30 min of sonication, and so we were interested in determining the corresponding $2-\theta$ shift, for the samples sonicated at 30 min. Interestingly, the greatest shift in $2-\theta$ was indeed observed within the initial 30 min of sonication for MoS_2 , WS_2 , and graphite. These all show a shift toward the compressive side (left) initially at $t_{sonic} = 30 \text{ min}$ as is evident from the magnified XRD spectra shown in Fig. 3b for the (103) crystal plane at $2-\theta = 39.42^\circ$ for MoS_2 , (d) the (103) crystal plane at $2-\theta = 39.46^\circ$ for WS_2 , and (f) the (002) crystal plane at $2-\theta = 26.38^\circ$ for graphite. However, for Al in Fig. 3h the (111) crystal plane at $2-\theta = 38.60^\circ$, experiences a negligible shift in the tensile direction after $t_{sonic} = 30 \text{ min}$. Unlike in the 2DLMs, after at $t_{sonic} = 30 \text{ min}$, the strain is in the opposite and compressive direction with $\Delta\theta = 0.24^\circ$, 0.24° and 0.29° , for MoS_2 , WS_2 and graphite, respectively, while for the non-layered material, Al, the $\Delta\theta = 0.02^\circ$ which is negligible, and incidentally also showed minimal changes in particle size or FR for $t_{sonic} = 30 \text{ min}$. After subjecting the samples to $t_{sonic} = 18 \text{ h}$, the change in $2-\theta$ in TMDCs was reduced and shifted toward the tensile (right) side, whereas the $2-\theta$ change in graphite persisted toward the compressive

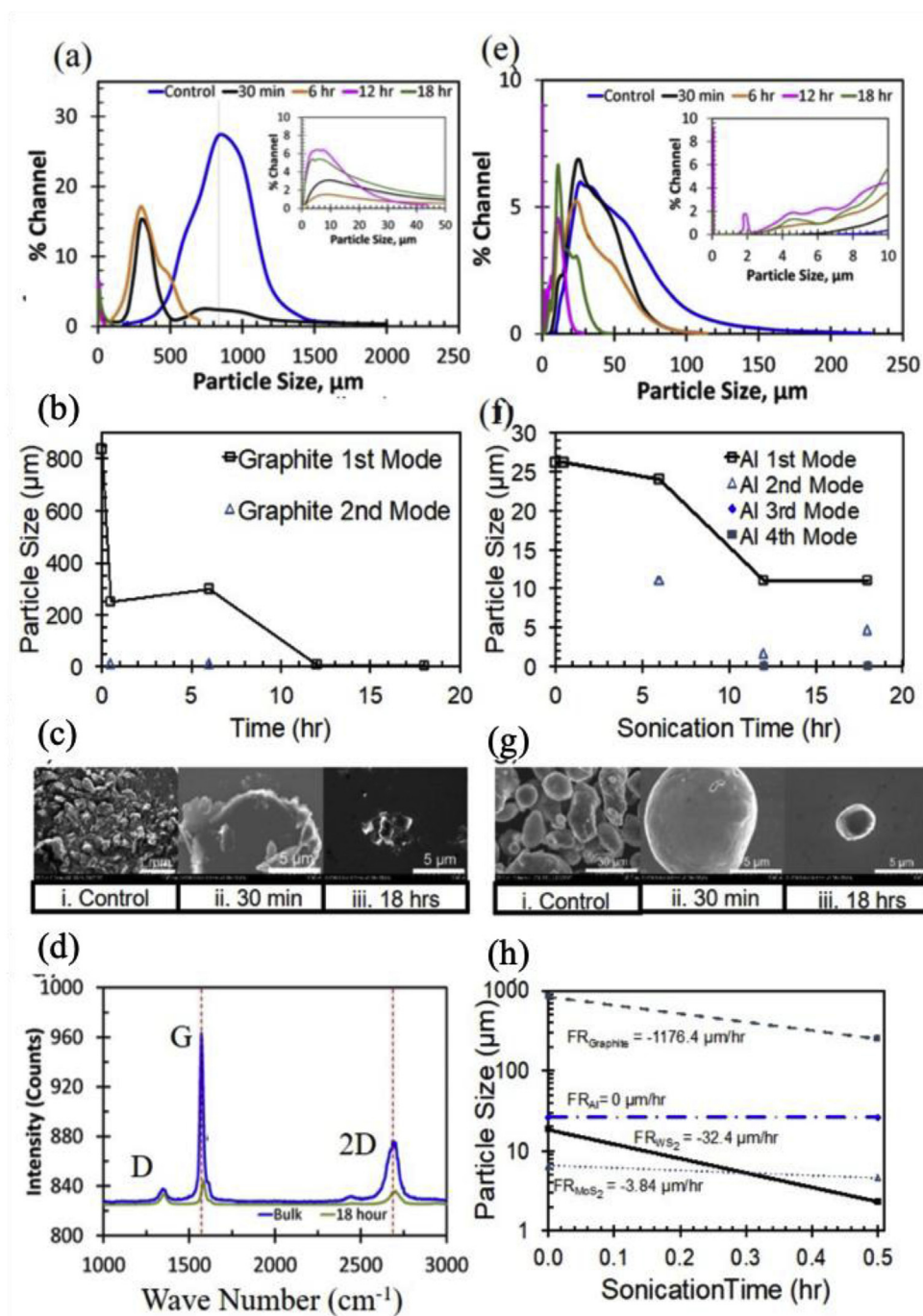


Fig. 2. Structural characterization of treated graphite powder shown in (a)–(d) while (e)–(g) refer to a non-layered material, Al nanoparticles. a) particle size distribution measured using the MicroTac for graphite; inset shows the peaks in the graphene distribution at lower length scales. b) S as a function of t_{sonic} showing the 1st and 2nd modes in the distribution. c) SEM micrographs showing a higher population of smaller particles in the background for the longer $t_{sonic} = 18$ h in (iii) compared to the control in (i). d) Raman spectra of the graphene dispersion where the well defined D, G and 2D peaks are seen, and the ratio of the 2D/G peak is < 2 , suggestive of multilayer graphene. Characterization of treated Al nanoparticles in (e)–(g). e) particle size distribution showing $S_{Al} \sim 26.16 \mu\text{m}$ for as received material and the inset shows the Al particle size over smaller length scales. f) S as a function of t_{sonic} showing the 1st, 2nd, 3rd and 4th modes. g) SEM micrographs showing the spherical morphology of the Al particles in (i)–(iii) as a function of t_{sonic} . h) Summary of the FR for all of the four materials analyzed during the initial 30 min of sonication. The $FR_{Al} \sim 0 \mu\text{m}\cdot\text{hr}^{-1}$ while the $FR_{Graphite}$ was $\sim -1176.4 \mu\text{m}\cdot\text{hr}^{-1}$, and the FR_{WS_2} and FR_{MoS_2} were determined to be $\sim -32.4 \mu\text{m}\cdot\text{hr}^{-1}$ and $-3.8 \mu\text{m}\cdot\text{hr}^{-1}$, respectively.

Table 1

Intensities of the D and G band peaks from the Raman spectra and D/G ratio for bulk and 18 h sonicated graphene samples.

	Bulk	18 h Sonication
Intensity of D band (I_D) – (a.u.)	838	834
Intensity of G band (I_G) – (a.u.)	964	843
D/G ratio	0.87	0.98

side, which is seen by the data in Fig. 3b, (d) and (f), respectively. On the other hand, Al showed a completely opposite response in contrast to the TMDCs and graphite, where the Al after $t_{sonic} = 18$ h, the 2θ peak shifted negligibly from the tensile direction toward a more significant shift of $\Delta\theta = 0.10^\circ$ (compressive). Thus, it appears that the XRD data correlates to the FR data obtained here, providing further insights into

the structural changes arising in the 2DLMs as a result of sonication.

2.2. Hybrid composite materials

The material characterization analysis for MoS_2 , WS_2 , graphite and Al powders provided insights into the structural and morphological changes occurring in these materials as a function of sonication time. We then proceeded to infuse these treated powders with other dissimilar materials, specifically flexible and stretchable elastomeric polyisoprene, and an optically transparent and flexible acrylic, poly-methyl-meth-acrylate (PMMA). Prior work [36] on the formation of hybrid structures with graphene and stretchable elastomers has shown that the uptake of the graphene into the elastomer is a diffusion-limited process; the smaller the size of the particulates, the more it is likely to impregnate deeper into the host matrix. Specifically, the extent of the

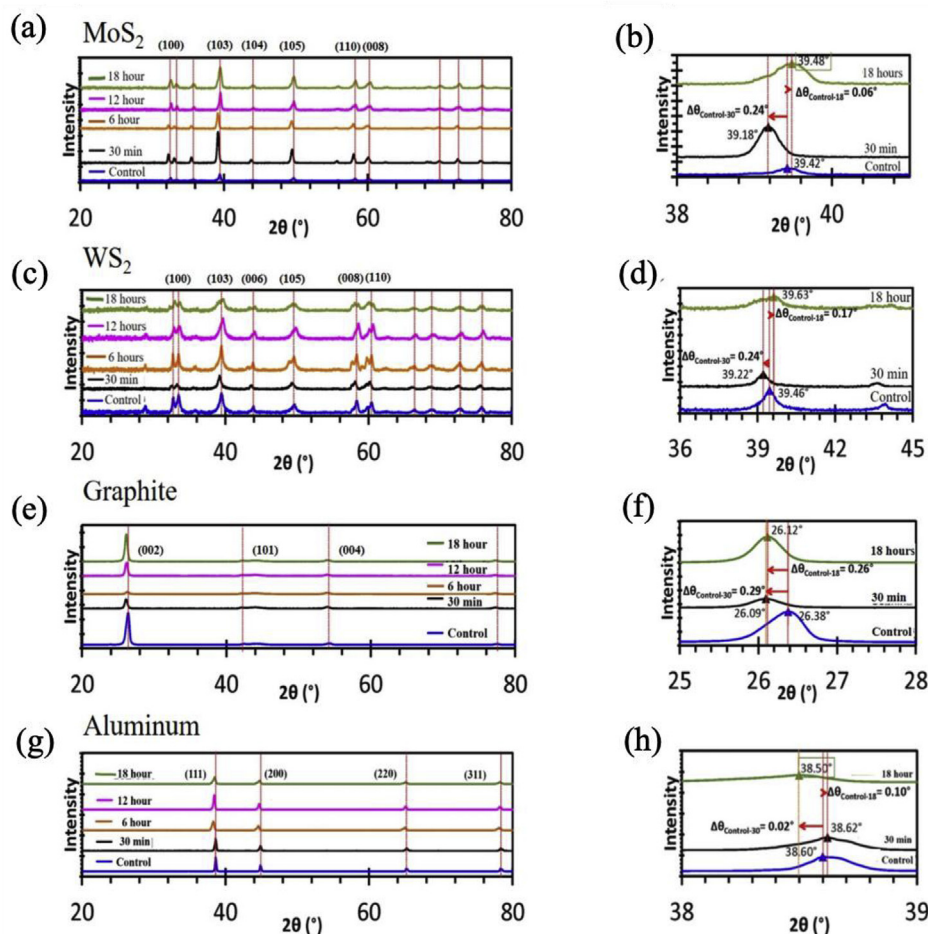


Fig. 3. (a)–(h) represent the XRD spectra for all of the four materials analyzed showing the unsonicated control sample, and comparison to the spectra obtained for the four sonicated times used. Complete XRD spectra for (a) MoS₂, (c) WS₂, (e) graphite, and (g) Al. The peaks for each material on the right in (b), (d), (f) and (h) show magnified views of a single crystal plane to quantify the shift in compressive or tensile stress. The magnified XRD spectra shown in (b) for the (103) crystal plane at $2-\theta = 39.42^\circ$ for MoS₂, (d) the (103) crystal plane at $2-\theta = 39.46^\circ$ for WS₂, and (f) the (002) crystal plane at $2-\theta = 26.38^\circ$ for graphite. For Al in (h) the (111) crystal plane at $2-\theta = 38.60^\circ$ experiences a negligible shift in the tensile direction after $t_{sonic} = 30$ min. Unlike in the 2DLMs, after $t_{sonic} = 30$ min, the strain is in the opposite and compressive direction with $\Delta\theta = 0.24^\circ$, 0.24° , and 0.29° , for MoS₂, WS₂ and graphite, respectively, while for the non-layered material, Al, the $\Delta\theta = 0.02^\circ$ which is negligible, and incidentally also showed minimal changes in FR for $t_{sonic} = 30$ min. In contrast, after $t_{sonic} = 18$ h for Al, the $2-\theta$ peak shifted negligibly from the tensile direction toward a more significant shift of $\Delta\theta = 0.10^\circ$ on the compressive side.

diffusion depends on particle size, where the diffusion coefficient D was computed to be $\sim 2.5 \times 10^{-12} \text{ m}^2\text{s}^{-1}$ [37], which is 100X lower compared to the D measured for small molecules diffusing into polyisoprene-based composites where $D > 10^{-10} \text{ m}^2\text{s}^{-1}$ [36]. Thus, in our dispersions, the samples sonicated for the longest duration, i.e. $t_{sonic} = 18$ h, had the greatest likelihood of diffusing deeper into the interior of the host matrix, rather than adsorbing merely on the surface. Therefore, these highly sonicated samples were then utilized and infused with the host matrix for the formation of the composites.

While developing the polyisoprene-based composites, the dispersion of the treated powder in the composite was not uniform, except for the graphite-polyisoprene composite, which was homogeneously dispersed and also yielded electrically conducting samples for which we present the data shortly. For the PMMA-based composites, a hardener was used in conjunction with the acrylic to solidify the sample. Other than the PMMA-graphene composites that were well formed and enabled us to measure the optical and electrical strain-dependent characteristics which we report here, the MoS₂, WS₂ and Al hybrid-PMMA composites on the other hand, were either not electrically conducting, or in the case of MoS₂ and WS₂, the composites did not solidify and remained highly viscous. For the PMMA-graphene composites, electrical measurements were obtained as a function of mechanical deformation, where silver paste (Pelco® Conductive Silver Paint, Product No:16062) was used to contact the samples. Besides the I–V measurements, optical measurements were also conducted as a function of mechanical strain induced through bending in the PMMA-graphene composites, which is discussed in more detail in Section 2.2.1.

2.2.1. Optical measurements

In order to conduct our strain-dependent analysis, 3D printed fixtures were designed, where each fixture had a unique radius of curvature ρ , as shown by the schematics in Fig. 4a (i)–(vi) where ρ_∞ was the control or unstrained sample, and ρ_5 , ρ_4 , ρ_3 , ρ_2 and ρ_1 represent increasing mechanical strain or decreasing radii of curvature. The strain-dependent optical measurements of the hybrid PMMA-graphene composites were conducted using the CARY 5000 Spectrophotometer in the absorption mode (described in the “Experimental Section”) using the fixtures shown in Fig. 4a(i)–(vi). Shown in Fig. 4b are optical images of the fabricated composites prior to mounting them in the fixtures. The optical absorption data are shown in Fig. 4c at $\lambda = 550$ nm for four graphene loadings, specifically $250 \text{ mg}\cdot\text{ml}^{-1}$, $300 \text{ mg}\cdot\text{ml}^{-1}$, $350 \text{ mg}\cdot\text{ml}^{-1}$, and $400 \text{ mg}\cdot\text{ml}^{-1}$ as a function of ρ . From this data, three distinct regimes are apparent, as shown in Fig. 4c, where Region I and Region III show the absorption to be insensitive to mechanical strain regardless of loading level. However, for lower loadings ($250 \text{ mg}\cdot\text{ml}^{-1}$ and $300 \text{ mg}\cdot\text{ml}^{-1}$) a minimum in absorption is seen for ρ_4 and ρ_3 in Region II, and the absorption then again recovers to its initial value for ρ_2 and ρ_1 . These characteristics resemble those of opto-mechanical filters, where the pathways for light “leakage” are enhanced in specific regimes, e.g. Region II, and some light is transmitted amidst the graphene platelets within a certain window of mechanical deformation. However, when the graphene loading is increased further, the optical response is largely unperturbed over all of the strain levels tested, as shown in Fig. 4c, for the 350 mg and 400 mg loadings. These results are conceptualized on the model proposed in Fig. 4d and (e) which represent scenarios for low and high loading, respectively. Here, the composite experiences two stress modes, the first in tension at the top surface of

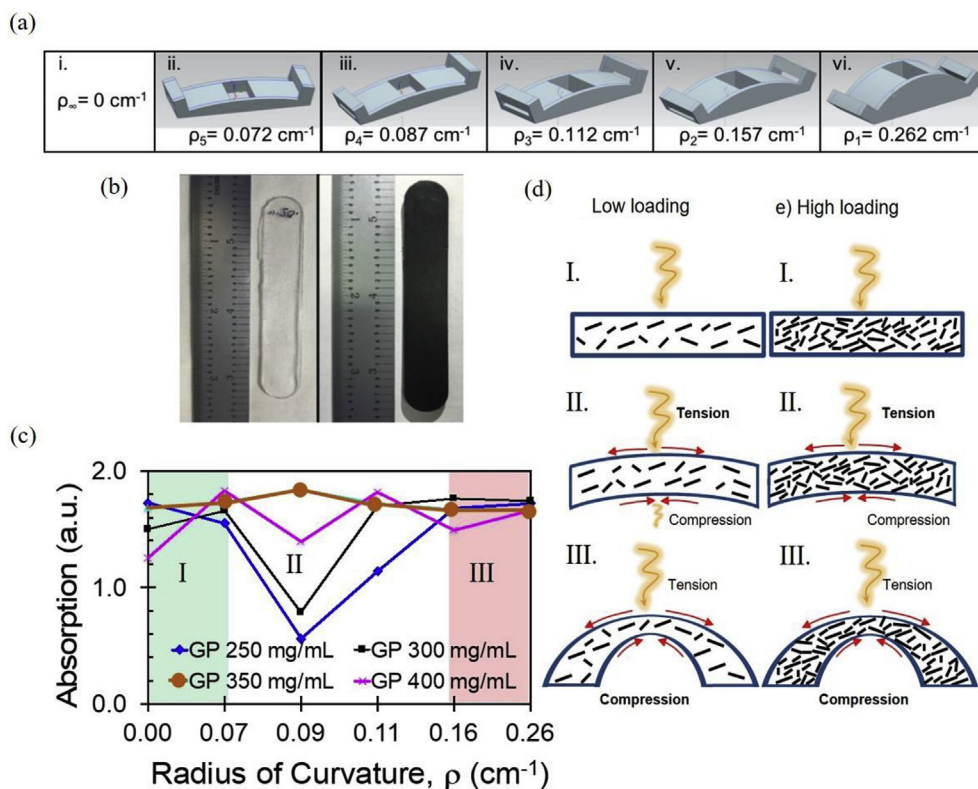


Fig. 4. a) Schematic layout of the fixtures designed inhouse using 3D printing to conduct the strain-dependent bending measurements on the PMMA-graphene composites. Shown are the fixtures for (i) ρ_{∞} (control or unstrained case) and (ii)-(vi) show ρ_5 , ρ_4 , ρ_3 , ρ_2 and ρ_1 , respectively and represent increasing mechanical strain or decreasing radii of curvature. b) Control sample (left image) showing the optically transparent PMMA without the graphene filler, while an example of the PMMA-graphene composite sample is shown on the right. c) Optical absorption measurements as a function of bending made at $\lambda = 550 \text{ nm}$ for the PMMA-graphene composites for four graphene powder (GP) loadings, where Region I and Region III show the absorption to be insensitive to mechanical strain regardless of loading. However, for lower loadings ($250 \text{ mg}\cdot\text{ml}^{-1}$ and $300 \text{ mg}\cdot\text{ml}^{-1}$), a minimum in absorption is seen for ρ_4 and ρ_3 , in Region II and the absorption then again recovers to its initial value for ρ_2 and ρ_1 , validating the opto-mechanical filtering response, where the pathways for light “leakage” are enhanced at certain loadings and strain levels. A model proposed in (d) and (e) for *low* and *high* graphene loading scenarios, respectively. Here, the composite experiences two stress or strain modes, the first in tension at

the top surface of the composite, and the second in compression on the underside. For the *low* loading case (d)-(II), for ρ_4 and ρ_3 , the absorption decreases, implying that the tensile mode on the top surface dominates, creating separation between graphene platelets, and pathways for light leakage within the composite until its exit on the undersurface. With further bending (d)-(III), the compressive mode is now active and the 2D layered morphology of the graphene platelets then causes those pathways to be diminished, since the platelet separation on this side is now decreased due to the compressive nature of the stresses, which increases optical absorption once again as depicted in Region III of (c). In the case of the *higher* loadings ($350 \text{ mg}\cdot\text{ml}^{-1}$ and $400 \text{ mg}\cdot\text{ml}^{-1}$) the optical response of the PMMA-graphene composite was insensitive to mechanical strain for all of the strains tested, which is visualized in the pictorial of (e)-(I)-(III), where the higher loading prevents any light leakage pathways through the composite, yielding a strain invariant optical absorber.

the composite, and the second in compression on the underside. For the *low* loading case (Fig. 4d (II)), the absorption decreases, i.e. ρ_4 and ρ_3 , implying that the tensile mode on the top surface dominates, creating separation between graphene platelets, and enhancing pathways for light leakage within the composite until its exit on the undersurface. With further bending (Fig. 4d-(III)), the compressive mode is now active and the 2D layered morphology of the graphene nanomembranes then causes those pathways to be continuous, since the platelet separation on this side is now decreased due to the compressive nature of the stresses, which increases optical absorption once again, as depicted in Region III of Fig. 4c. In the case of the *higher* loadings ($350 \text{ mg}\cdot\text{ml}^{-1}$ and $400 \text{ mg}\cdot\text{ml}^{-1}$) the optical response of the PMMA-graphene composite was insensitive to mechanical strain for all of the strains tested, which is visualized in the schematic model of Fig. 4e-(I)-(III), exhibiting characteristics of a strain-invariant optical absorber. These results show the potential of forming opto-mechanical filters using 2D PMMA-graphene composites, where the filtering is engineered through the graphene loading as well as mechanical strain.

2.2.2. Electrical properties

The electrical properties of the graphene composites were tested as a function of mechanical strain in bending mode for the PMMA-graphene matrix, as well as in stretching-mode for the flexible and stretchable polyisoprene-graphene matrix. We first describe the results of the former, where the data are shown in Fig. 5 at the same graphene loadings tested previously for the optical measurements (Fig. 4). The data in Fig. 5a, (b), (c), and (d) are I-V Characteristics for the four graphene loadings, $\sim 250 \text{ mg}\cdot\text{ml}^{-1}$, $300 \text{ mg}\cdot\text{ml}^{-1}$, $350 \text{ mg}\cdot\text{ml}^{-1}$, and $400 \text{ mg}\cdot\text{ml}^{-1}$, respectively, as a function of mechanical strain for ρ_{∞} , ρ_5 ,

ρ_4 , ρ_3 , ρ_2 and ρ_1 . As in the strain-dependent optical measurements, the I-V response also showed a distinct behavior for the *low* loading case (i.e. 250 and $300 \text{ mg}\cdot\text{ml}^{-1}$), in contrast to the *higher* graphene loadings (i.e. $350 \text{ mg}\cdot\text{ml}^{-1}$ and $400 \text{ mg}\cdot\text{ml}^{-1}$). In the *low* loading case, the I-V response in Fig. 5a and (b) shows the evolution from the non-Ohmic (non-linear) to the Ohmic (linear) scenario as strain increases. In contrast, for the *higher* loading case, the I-V response in Fig. 5c and (d) shows the evolution from an Ohmic to a non-Ohmic character as strain increases. The explanation for this strain-dependent response of the electrical transport for various loadings is explained on the basis of percolation theory. It is well understood from Balberg et al. [38] that percolation theory is operative in conductive composites, and that at low loadings of the conductive filler in the non-conducting host matrix, transport occurs via tunneling or hopping since nearest neighbor particles are not necessarily in direct physical contact. As the concentration of the conducting filler increases within the host, or reaches the so-called “percolation threshold”, the conducting particles in the host matrix are physically connected, and form Ohmic conduction pathways for electrical transport [38]. Therefore, below the percolation threshold, electrical transport in the hybrid composites occurs via hopping of electrons and tunneling, and above the percolation threshold, electrical transport occurs via direct physical contact and hence is Ohmic.

As a result, the strain-dependent electrical transport data in Fig. 5a and (b) are suggestive of graphene loading to be below the percolation threshold. Hence, in the unstrained (unbent) case, electrical transport is via tunneling (Fig. 5e left) which explains the non-Ohmic I-V response in Fig. 5a and (b). However, as bending or strain are induced, the transition from the electron hopping and tunneling regime now evolves into direct contact and hence the transport now also has an Ohmic

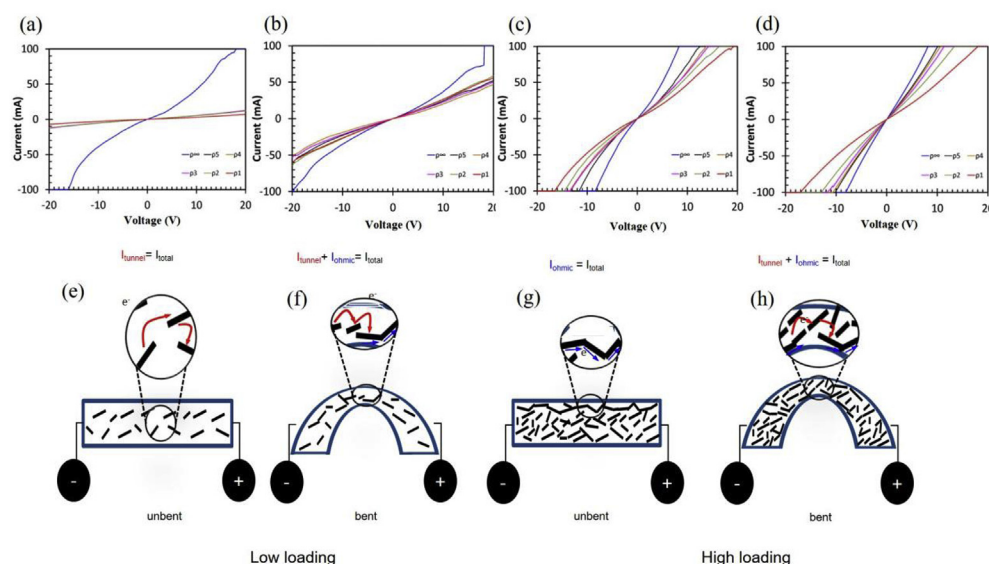


Fig. 5. I-V response of the PMMA-graphene composite with graphene/graphite loading of **a)** 250 mg·ml⁻¹, **b)** 300 mg·ml⁻¹, **c)** 350 mg·ml⁻¹ and **d)** 400 mg·ml⁻¹ at the six radii of curvature depicted by the schematics in Fig. 4a – (i)-(vi). The low loading case in (a) and (b) shows the response to be non-Ohmic (non-linear) in the absence of strain which evolves toward the Ohmic regime (i.e. I-V linear) with bending. For the higher loading cases in (c) and (d), the response is Ohmic in the absence of bending but evolves toward a non-Ohmic regime with increasing strain. The distance between the W probes was fixed to 1 cm. A model is put forth in (e) and (f) that represents the electron flow which is presumed to arise from a tunneling or electron hopping mechanism (represented by red arrows) and an Ohmic transport (represented by blue arrows) for graphene-graphene platelets in direct physical contact. At low graphene filler loadings, the

transport is dominated by tunneling pathways and hopping of electrons since the composite is below the percolation threshold, and hence the contribution to I_{total} is mainly from I_{tunnel} . For the unbent or unstrained case in (e)-left. In the strained or bent case in (e)-right, the graphene-graphene platelets are under compressive stresses on the underside and likely to touch which leads to Ohmic transport with bending. In (f) at the higher loading, the contribution is primarily from direct Ohmic contact in the unbent or unstrained case, which explains the Ohmic response seen in the I-V Characteristic. As bending or strain is induced in (f)-right, the conducting channels are broken and there are contributions from tunneling pathways or a hopping mechanism, which explains the non-linear character seen with loading in the bent or strained case. (For interpretation of the references to colour in this figure legend, the reader is referred to the Web version of this article.)

contribution (Fig. 5e, right). Thus, the model depicted in Fig. 5e shows the total current I_{total} to be largely determined by a contribution from the tunneling and hopping current I_{tunnel} in the unstrained case, while in the bent case, I_{total} is a sum of I_{tunnel} and I_{ohmic} . This explains the non-linear I-V response for low loadings seen at low bias voltages, which then progresses more toward a linear or Ohmic regime as bending occurs. Now for the case of higher loadings (350 mg·ml⁻¹ and 400 mg·ml⁻¹), the density of the graphene platelets is high and thus there is an enhanced probability of graphene-graphene platelets being in direct contact which leads to an Ohmic response in the unstrained or unbent case, as shown in Fig. 5c and (d). In the unstrained or unbent case, the I_{total} is largely determined by the I_{ohmic} contribution, which can be visualized in Fig. 5f (left). However, as strain or bending are induced, the separation between the graphene-graphene platelets increases on the top-side of the composite sample where tensile forces are dominant, and the electrical transport now migrates from Ohmic to non-Ohmic, while on the underside compressive forces are present which decrease separation between graphene platelets and the contribution from the Ohmic response is still present. The I_{total} once again for the strained case at high loading is then a sum of the I_{tunnel} and I_{ohmic} . This scenario is visualized by the schematic in Fig. 5f (right).

We now revisit our discussion on the percolative composites formed using an elastic, stretchable polymer, polyisoprene, which is the main matrix material in commercially available rubber bands. The strain-dependent electrical transport measurements on hybrid polyisoprene-graphene composites are shown by the data in Fig. 6a, where the composites were formed using 37.5 mg·ml⁻¹ and 75.5 mg·ml⁻¹ of graphene loadings in NMP. Strain in the composites was induced through stretching using an in-house designed fixture, which is shown schematically in the inset of Fig. 6a. Unlike the PMMA-graphene composites, the I-V response of the polyisoprene-graphene composites showed an Ohmic behavior at all strain levels tested for both graphene loadings, where strain ranged up to 200%, as shown by the data in Fig. 6a. This is suggestive of the few-layer platelets formed using sonicated graphene infusing well into the polyisoprene matrix with a favorable diffusivity, since the Ohmic response is indicative of graphene-graphene contacts that are still dominant at strain levels up to 200%.

The specific current sensitivity for the 37.5 mg·ml⁻¹ loading was 0.90 μ A/% strain at 7 V, 0.65 μ A/% strain at 5 V and 0.39 μ A/% strain at 3 V, which were calculated from the data shown in Fig. 6b up to a strain level of 50%. For the higher concentration of 75 mg·ml⁻¹ the specific current sensitivity was 0.90 μ A/% strain at 7 V, 0.64 μ A/% strain at 5 V and 0.38 μ A/% strain at 3 V, which implies that in terms of sensitivity (up to 50% strain), both loadings in the composites yield similar strain-dependent characteristics. The gauge factor for the low graphene concentration sample (37.5 mg·ml) was calculated to be \sim 75, and was the highest at 200% strain as shown in Fig. 6c. Our hybrid polyisoprene-graphene composites show a strain-dependent electrical modulation of current, akin to that observed in a piezoresistive material system. Hence these hybrid composites have utility in sensing applications, where the I-V data in Fig. 6d shows the modulation of the current response when the composite sample is placed on a finger to detect joint movement, where the various finger positions are depicted in Fig. 6e. These measurements shown in Fig. 6d were consistent with the I-V data gathered in Fig. 6a as a function of strain. As the finger was bent progressively from positions shown in Fig. 6e-(i) (no movement), to (ii) (first movement), (iii) (second movement), (iv) (third movement) and (v) (fourth movement), the I-V data in Fig. 6d shows a distinct difference at each of these joint movements. This data clearly shows the importance and utility of these hybrid 2D composites for yielding high gauge factor devices that work on the principle of piezoresistivity, which can be easily integrated into prototype devices to detect bodily movements such as those seen at joints, or in wearable electronics generally.

A comparative analysis between our as-prepared strain sensors was conducted with regard to other low-dimensionality materials integrated with polymers, as shown in the Summary Table 2. In surveying the literature, Lin et al. [39] used hybrid carbon fillers with a thermoplastic polyurethane (TPU) matrix which yielded gauge factors up to 140,238 where the exceptional performance was attributed to the untangled morphology of the carbon fillers. Shin et al. [40], reported on highly elastic (up to 300% strain), electrically conductive composite sheets by incorporating MWNT forests in a polyurethane (PU) binder matrix, where the high elasticity was believed to arise from the inherent property of the matrix binder. Other work has shown carbon nanotube

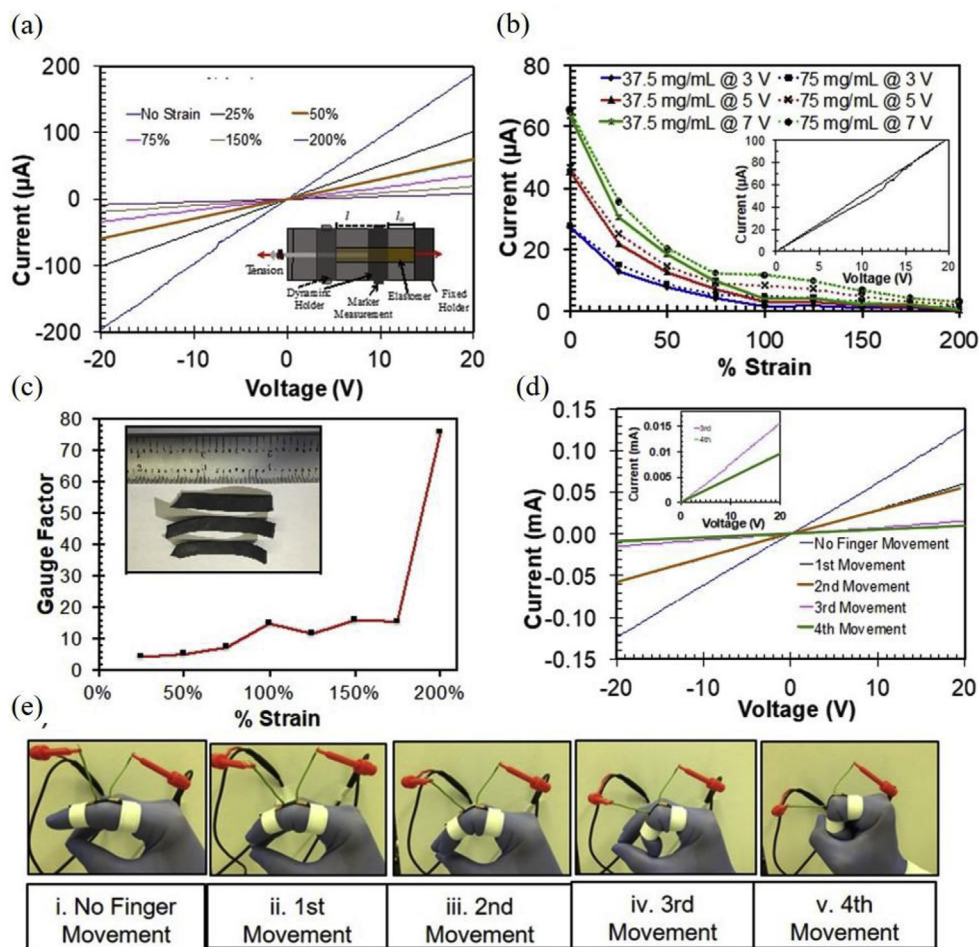


Fig. 6. (a) I–V response of the polyisoprene-graphene composite made using solutions dispersed at graphene loading of $37.5 \text{ mg}\cdot\text{ml}^{-1}$. The inset shows the schematic of the in house tensile test set up designed and used in these measurements. (b) The current as a function of % strain at 3 V, 5 V and 7 V for the samples made using graphene loadings of 37.5 and $75 \text{ mg}\cdot\text{ml}^{-1}$. The inset shows the degree of hysteresis present at 25% strain for the $75 \text{ mg}\cdot\text{ml}^{-1}$ case where good linearity is exhibited. (c) The gauge factor as a function of percent strain. The gauge factor for the polyisoprene-graphene composite with a concentration of $37.5 \text{ mg}\cdot\text{ml}^{-1}$ was computed to be ~ 75 at a strain level of 200%, which is 10X larger compared to gauge factors seen in conventional metal-foil based strain sensors. (d)–(e) data obtained from prototype demonstrations of engineered polyisoprene-graphene composites used in a practical platform for detecting bodily movements, e.g. at a finger joint. (d) The modulation of the current is clearly evident with finger movement from the I–V data, where the finger positions are shown in (e)–(i)–(v) for the case of no movement in (i), 1st movement in (ii), 2nd movement in (iii), 3rd movement in (iv) and 4th movement in (v). Inset shows modulation of current of last two movements (3rd and 4th) in greater detail. This prototype demonstration confirms the promise of 2D graphene-based composites for wearable electronics.

(CNTs) with PDMS promising for capacitive strain sensing with strains up to 300% [41]. A processing technique for naturally-derived supramolecular elastomers containing green synthesized silver nanofibers for self-repairing e-skin sensors reported by Yang et al. in 2019 [42] resulted in gauge factors of up to ~ 406 . In 2018, Song et al. [32] reported on biocompatible medical tapes and thin Au film based strain sensors to detect skin activity with strain levels up to 140% detectable and gauge factors ranging from 7.2 to 474.8. In 2016, Boland et al. [43] reported on a viscoelastic graphene–polymer nanocomposite sensor with a gauge factor of more than 500, and in prior work conducted by the same group in 2014 [36], liquid exfoliated graphene–natural rubber composites showed strain levels exceeding 800% with a gauge factor of 35, where prototype devices detected motions associated with

breathing and heart-beat. Functionalized graphene–polyvinylidene fluoride strain sensors reported by Eswaraiiah et al. in 2011 [44] demonstrated a light-weight, low-cost, flexible strain sensor where graphene loading as low as 2 wt% showed enhanced performance compared to CNT-based fillers. Graphene–TPU composites reported by Liu et al. in 2016 [45], demonstrated strain levels of up to 100 with a maximum gauge factor close to 18. While there are reports of polymer–low dimensionality material hybrid composites exhibiting strain levels and gauge factors higher than the work reported here, the current study is novel since our % strain levels and gauge factors are both competitive with previous work on 2DLM-based composites, where gauge factors tended to be below 35.

Table 2

Comparative analysis of % strain and gauge factors reported in this work in the context of the prior relevant literature on low-dimensionality materials infused with polymers for strain-based sensing. The results indicate that the composites used in this study are competitive with the current state-of-the-art for 2DLM-based strain sensors.

Hybrid Composite Strain-sensor	Strain (%)	Gauge Factor	Ref.
Functionalized multiwalled nanotubes (MWNTs) in thermoplastic polyurethane (TPU) based strain sensors	200	5–140,238	39
MWNT – polyurethane (PU) sheet sensors	300		40
Carbon nanotubes (CNT) – polydimethylsiloxane (PDMS) composite sensor	300		41
Green-synthesized 1D silver nanofibers (AgNFs) – naturally-derived supramolecular elastomer		405.6	42
Biocompatible medical tapes and thin Au films strain sensor for versatile skin activity recognition	140	7.2–474.8	32
Viscoelastic graphene – polymer nanocomposite		> 500	43
Liquid exfoliated graphene – natural rubber composite	> 800	Up to 35	36
Functionalized graphene – polyvinylidene fluoride strain sensors			44
Graphene–Thermoplastic Polyurethane (TPU) conductive polymer composites as strain sensors	100	0.78–17.7	45
Graphene–Polyisoprene and Polymethyl methacrylate (PMMA) composites for strain sensing	200	75	[This Work]

3. Conclusion

The effect of ultrasonication time on the structural characteristics of 2DLMs such as MoS₂, WS₂, and graphite was explored in the presence of NMP, and Al powder was also used for comparative analysis. A clear trend was seen with the 2DLMs which showed the greatest *FR* within the first 30 min of sonication, while the *FR*_{Al} was $\sim 0 \mu\text{m}\cdot\text{hr}^{-1}$. For the 2DLMs, the *FR*_{Graphite} was $\sim -1176.4 \mu\text{m}\cdot\text{h}^{-1}$, and the *FR*_{WS2} and *FR*_{MoS2} were determined to be $\sim -32.4 \mu\text{m}\cdot\text{hr}^{-1}$ and $-3.8 \mu\text{m}\cdot\text{hr}^{-1}$ respectively. Despite the fact that the *FR*_{MoS2} was the lowest, the Raman analysis however clearly indicated that the ensuing platelets were 2–3 layers thick, and suggested that the sonication conditions used were effective in shearing the bulk material into few layer crystallites. Such treated samples were infused into polymer matrix materials, specifically optical transparent PMMA and stretchable/flexible polyisoprene. Here, the strain-dependent opto-mechanical response for PMMA-graphene composite was measured in bending mode where an opto-mechanical filtering response was evident as a function of graphene loading and mechanical strain. For the PMMA-graphene composite, the electrical properties with bending were tested, where total current was found to be dependent on an Ohmic (direct contact) as well as a non-Ohmic component (due to tunneling) in these percolative composites. In addition, hybrid polyisoprene-graphene composites were implemented for flexible, stretchable strain-based sensing applications, where a piezoresistive response was evident. Such piezoresistive composites yielded a gauge factor of ~ 75 , and strain levels of $\sim 200\%$, where the gauge factors calculated were 10X higher compared to metal-foil based strain sensors. These materials were then implemented into strain-based sensing platforms to successfully demonstrate sensors that can detect bodily movement for wearable electronics. Our results affirm the attractive properties of solution processed 2DLMs which can pave the way for novel opto-electro-mechanical strain-based sensing devices emerging from these materials in the future.

4. Experimental

Preparation of 2DLM dispersions: As received powder materials of MoS₂ (Sigma Aldrich 69860-100G), WS₂ (Sigma Aldrich 243639-50G), Graphite (Alf Aesar 99.9% metal basis), and Al powder (Fisher Science Education Reagent Grade S25144) were ultrasonicated in NMP using a bath sonicator (Branson 4500H) at sonication times ranging from 0 min to 18 h. The powder was dispersed at a concentration of $37.5 \text{ mg}\cdot\text{ml}^{-1}$ of NMP. For maximal sample reliability, MoS₂, WS₂, graphite and Al powder dispersions were divided into five different sample sets, and each sample was exposed to the various sonication times noted.

Particle Size Measurement using Optical Interferometry: Particle size measurements were conducted using the MicroTrac S3500 (Bluewave Model). The treated powder is dispersed in IPA for measurements to be conducted in the MicroTrac, where three lasers (two blue and one red laser) are focused onto the sample and a light scattering technique is used to compute the particulate size in the range of 0.02–2800 μm . The red laser scatters light from 0 to 60° to acquire the scattered signal from the larger particles, while the blue lasers are responsive to smaller sized particulates in the sub-micron and nm-scale regime.

Preparation of the graphene-elastomer composites: Samples of graphite/graphene were formed at two loadings of graphene, $37.5 \text{ mg}\cdot\text{ml}^{-1}$ and $75 \text{ mg}\cdot\text{ml}^{-1}$. For the polyisoprene-graphene composites, experimental methods as outlined in Ref. 34 were used, where the polyisoprene material was soaked in toluene for 3.5 h to allow it to swell and expand. The polyisoprene samples were then immersed in the ultrasonicated graphene-NMP dispersions for 48 h where the graphene platelets impregnate the polyisoprene matrix. Finally, the composites were allowed to dry at 60 °C for 72 h to drive off the NMP and water. Electrical measurements on the composites were then conducted as a function of mechanical strain, where silver paste was used to make

electrical contacts to the composites. A custom-built fixture was designed for conducting the strain-dependent measurements in tension (schematic of the fixture is shown in the inset of Fig. 6a).

Preparation of the graphene-acrylic composites: Acrylic-based PMMA composites were formed through the incorporation of graphene powder sonicated for 18 h at loadings of 250, 300, 350 and $400 \text{ mg}\cdot\text{ml}^{-1}$ in 3 ml of PMMA solution. The solutions were mixed thoroughly and poured into custom-designed molds with length, width and thickness of 2.5 inches (6.35 cm), 0.5 inches (1.27 cm), and 0.05 inches (0.127 cm), respectively. Casting of the PMMA-graphene composite samples was enabled by the addition of several drops of hardener to solidify the samples, after which point they were dried overnight at room temperature and allowed to harden further at ambient conditions.

Acknowledgement

We greatly appreciate the support received from the Army Research Office (grant number W911NF-15-1-0425) that enabled us to pursue this work. A.B.K. is also grateful to the support received from the UNT start-up package for helping establish the Nanoscale Materials and Devices Laboratory and the PACCAR Endowed Professorship and Institute support. ADM acknowledges the LDRD program at LANL for the funding. The research was performed, in part, at the Center for Integrated Nanotechnologies, an Office of Science User Facility operated for the U.S. Department of Energy (DOE) Office of Science. Los Alamos National Laboratory, an affirmative action equal opportunity employer, is operated by Los Alamos National Security, LLC, for the National Nuclear Security Administration of the U.S. Department of Energy under contract DE-AC52-06NA25396.

Appendix A. Supplementary data

Supplementary data to this article can be found online at <https://doi.org/10.1016/j.compscitech.2019.107687>.

References

- [1] K.S. Novoselov, A.K. Geim, S. V. Morozov, D. Jiang, Y. Zhang, S. V. Dubonos, I. V. Grigorieva, A.A. Firsov, Electric field effect in atomically thin carbon films, *Science* 306 (2004) 666–669.
- [2] A.K. Geim, Graphene: status and prospects, *Science* 324 (2009) 1530–1535.
- [3] P. Matyba, H. Yamaguchi, G. Eda, M. Chhowalla, L. Edman, N.D. Robinson, Graphene and mobile ions: the key to all-plastic, solution-processed light-emitting devices, *ACS Nano* 4 (2010) 637–642.
- [4] K.S. Novoselov, V.I. Fal'ko, L. Colombo, P.R. Gellert, M.G. Schwab, K. Kim, A roadmap for graphene, *Nature* 490 (2012) 192–200.
- [5] E.W. Hill, A.K. Geim, K. Novoselov, F. Schedin, P. Blake, Graphene spin valve devices, *IEEE Trans. Magn.* 42 (2006) 2694–2696.
- [6] H.B. Heersche, P. Jarillo-Herrero, J.B. Oostinga, L.M.K. Vandersypen, A.F. Morpurgo, Bipolar supercurrent in graphene, *Nature* 446 (2007) 56–59.
- [7] Q.H. Wang, K. Kalantar-Zadeh, A. Kis, J.N. Coleman, M.S. Strano, Electronics and optoelectronics of two-dimensional transition metal dichalcogenides, *Nat. Nanotechnol.* 7 (2012) 699–712.
- [8] A.B. Kaul, Two-dimensional layered materials: structure, properties, and prospects for device applications, *J. Mater. Res.* 29 (2014) 348–361.
- [9] D. Jariwala, V.K. Sangwan, L.J. Lauhon, T.J. Marks, M.C. Hersam, Emerging device applications for semiconducting two-dimensional transition metal dichalcogenides, *ACS Nano* 8 (2014) 1102–1120.
- [10] A.K. Geim, K.S. Novoselov, The rise of graphene, *Nat. Mater.* (2007) 183–191.
- [11] A.D. Wilson, J.A. Yoffe, The transition metal dichalcogenides: discussion and interpretation of the observed optical, electrical and structural properties[†], *Adv. Phys.* 18 (1969) 193–335.
- [12] O.M.J. van't Erve, A.T. Hanbicki, A.L. Friedman, K.M. McCreary, E. Cobas, C.H. Li, J.T. Robinson, B.T. Jonker, Graphene and monolayer transition-metal dichalcogenides: properties and devices, *J. Mater. Res.* 31 (2016) 845–877.
- [13] J.N. Coleman, M. Lotya, A. O'Neill, S.D. Bergin, P.J. King, U. Khan, K. Young, A. Gaucher, S. De, R.J. Smith, I.V. Shvets, S.K. Arora, G. Stanton, H.-Y. Kim, K. Lee, G.T. Kim, G.S. Duesberg, T. Hallam, J.J. Boland, J.J. Wang, J.F. Donegan, J.C. Grunlan, G. Moriarty, A. Shmeliov, R.J. Nicholls, J.M. Perkins, E.M. Grieveson, K. Theuwissen, D.W. McComb, P.D. Nellist, V. Nicolosi, Two-Dimensional nanosheets produced by liquid exfoliation of layered materials, *Science* 331 (2011) 568–571.
- [14] U. Khan, A. O'Neill, M. Lotya, S. De, J.N. Coleman, High-concentration solvent exfoliation of graphene, *Small* 6 (2010) 864–871.

- [15] G. Cunningham, M. Lotya, C.S. Cucinotta, S. Sanvito, S.D. Bergin, R. Menzel, M.S.P. Shaffer, J.N. Coleman, "Solvent exfoliation of transition metal dichalcogenides: dispersability of exfoliated nanosheets varies only weakly between compounds solvent exfoliation of transition metal dichalcogenides: dispersability of exfoliated nanosheets varies only weakly bet", *ACS Nano* 6 (2012) 3468–3480.
- [16] H. Tao, Y. Zhang, Y. Gao, Z. Sun, C. Yan, J. Texter, "Scalable exfoliation and dispersion of two-dimensional materials – an update", *Phys. Chem. Chem. Phys.* 19 (2017) 921–960.
- [17] A. Jawaid, D. Nepal, K. Park, M. Jespersen, A. Qualley, P. Mirau, L.F. Drummy, R.A. Vaia, Mechanism for liquid phase exfoliation of MoS₂, *Chem. Mater.* 28 (2016) 337–348.
- [18] B.J. Carey, T. Daeneke, E.P. Nguyen, Y. Wang, Two solvent grinding sonication method for the synthesis of two-dimensional tungsten disulphide flakes, *Chem. Commun.* 51 (2015) 3770–3773.
- [19] S. Stankovich, R.D. Piner, X. Chen, N. Wu, S.T. Nguyen, R.S. Ruoff, Stable aqueous dispersions of graphitic nanoplatelets via the reduction of exfoliated graphite oxide in the presence of poly(sodium 4-styrenesulfonate), *J. Mater. Chem.* 16 (2006) 155–158.
- [20] S. Stankovich, D.A. Dikin, G.H.B. Dommett, K.M. Kohlhaas, E.J. Zimney, E.A. Stach, R.D. Piner, S.T. Nguyen, R.S. Ruoff, Graphene-based composite materials, *Nature* 442 (2006) 282–286.
- [21] Y. Hu, X. Li, A. Lushington, M. Cai, D. Geng, M.N. Banis, R. Li, X. Sun, Fabrication of MoS₂-Graphene nanocomposites by layer-by-layer manipulation for high-performance lithium ion battery anodes, *ECS J. Solid State Sci. Technol.* 2 (2013) M3034–M3039.
- [22] H.J. Conley, B. Wang, J.I. Ziegler, R.F. Haglund, S.T. Pantelides, K.I. Bolotin, Bandgap engineering of strained monolayer and bilayer MoS₂, *Nano Lett.* 13 (2013) 3626–3630.
- [23] L. Tao, H. Long, B. Zhou, S.F. Yu, S.P. Lau, Y. Chai, K.H. Fung, Y.H. Tsang, J. Yao, D. Xu, Preparation and characterization of few-layer MoS₂ nanosheets and their good nonlinear optical responses in the PMMA matrix, *Nanoscale* 6 (2014) 9713–9719.
- [24] S. Yao, Y. Zhu, Wearable multifunctional sensors using printed stretchable conductors made of silver nanowires, *Nanoscale* 6 (2014) 2345.
- [25] M. Kaltenbrunner, T. Sekitani, J. Reeder, T. Yokota, K. Kuribara, T. Tokuhara, M. Drack, R. Schwödiauer, I. Graz, S. Bauer-Gogonea, S. Bauer, T. Someya, An ultralightweight design for imperceptible plastic electronics, *Nature* 499 (2013) 458–463.
- [26] T. Yamada, Y. Hayamizu, Y. Yamamoto, Y. Yomogida, A. Izadi-Najafabadi, D.N. Futaba, K. Hata, A stretchable carbon nanotube strain sensor for human-motion detection, *Nat. Nanotechnol.* 6 (2011) 296–301.
- [27] M. Amjadi, A. Pichitpajongkit, S. Lee, S. Ryu, I. Park, Highly stretchable and sensitive strain sensor based on silver nanowire-elastomer nanocomposite, *ACS Nano* 8 (2014) 5154–5163.
- [28] M. Hempel, D. Nezhich, J. Kong, M. Hofmann, A novel class of strain gauges based on layered percolative films of 2D materials, *Nano Lett.* 12 (2012) 5714–5718.
- [29] J. Botsis, L. Humbert, F. Colpo, P. Giaccari, Embedded fiber Bragg grating sensor for internal strain measurements in polymeric materials, *Optic Laser. Eng.* 43 (2005) 491–510.
- [30] T. Yamada, Y. Hayamizu, Y. Yamamoto, Y. Yomogida, A. Izadi-Najafabadi, D.N. Futaba, K. Hata, A stretchable carbon nanotube strain sensor for human-motion detection, *Nat. Nanotechnol.* 6 (2011) 296–301.
- [31] S.P. Beeby, G. Ensel, M. Kraft, N.M. White, MEMS Mechanical Sensors, Artech House, Boston, 2004.
- [32] Z. Song, W. Li, Y. Bao, F. Han, L. Gao, J. Xu, Y. Ma, D. Han, L. Niu, "Breathable and skin-mountable strain sensor with tunable stretchability, sensitivity and linearity via surface strain delocalization for versatile skin activities' recognition", *ACS Appl. Mater. Interfaces* 10 (2018) 42826–42836.
- [33] H. Zeng, G. Liu, J. Dai, Y. Yan, B. Zhu, R. He, L. Xie, S. Xu, X. Chen, W. Yao, X. Cui, Optical signature of symmetry variations and spin-valley coupling in atomically thin tungsten dichalcogenides, *Sci. Rep.* 3 (2013) 1608.
- [34] C. Rice, R.J. Young, R. Zan and U. Bangert, "Raman-scattering measurements and first-principles calculations of strain-induced phonon shifts in monolayer MoS₂", *Phys. Rev. B*; 87(081307), 1 – 5, (2013).
- [35] L.G. Cancado, A. Jorio, E.H. Martins, F. Ferreira, C.A. Stavale, C.A. Achete, R.B. Capaz, M.V.O. Moutinho, A. Lombardo, T.S. Kulmala, A.C. Ferrari, Quantifying defects in graphene via Raman spectroscopy at different excitation energies, *Nano Lett.* 11 (2011) 3190.
- [36] C.S. Boland, U. Khan, C. Backes, A. O'Neill, J. McCauley, S. Duane, R. Shanker, Y. Liu, I. Jurewicz, A.B. Dalton, J.N. Coleman, Sensitive, high-strain, high-rate bodily motion sensors based on graphene-rubber composites, *ACS Nano* 8 (2014) 8819–8830.
- [37] H.C. Obasi, O. Ogbobe, I.O. Igwe, Diffusion characteristics of toluene into natural rubber/linear low density polyethylene blends, *Int. J. Polym. Sci.* 2009 (2009).
- [38] I. Balberg, D. Azulay, D. Tokor, O. Millo, Percolation and tunneling in composite materials, *Int. J. Mod. Phys. B* 18 (2004) 2091–2121.
- [39] L. Lin, S. Liu, Q. Zhang, X. Li, M. Ji, H. Deng, Q. Fu, Towards tunable sensitivity of electrical property to strain for conductive polymer composites based on thermoplastic elastomer, *ACS Appl. Mater. Interfaces* 5 (2013) 5815–5824.
- [40] M.K. Shin, J. Oh, M. Lima, M.E. Kozlov, S.J. Kim, H. Baughman, Elastomeric conductive composites based on carbon nanotube forest, *Adv. Mater.* 22 (2010) 2663–2667.
- [41] L. Cai, L. Song, P. Luan, Q. Zhang, N. Zhang, Q. Gao, D. Zzhao, X. Zhang, M. Tu, F. Yang, W. Zhou, Q. Fan, J. Lou, W. Zhou, P.M. Ajayan, S. Xie, Super-stretchable, transparent carbon nanotube-based capacitive strain sensors for human motion detection, *Sci. Rep.* 3 (2013) 3048.
- [42] Y. Yang, J. Liu, J. Cao, Z. Zhou, X. Zhang, A naturally-derived supramolecular elastomer containing green-synthesized silver nanofibers for self-repairing E-skin sensor, *J. Mater. Chem. C* 7 (2019) 578–585.
- [43] C.S. Boland, U. Khan, G. Ryan, S. Barwich, R. Charifou, A. Harvey, C. Backes, Z. Li, M.S. Ferreira, M.E. Möbius, R.J. Young, J.N. Coleman, Sensitive electromechanical sensors using viscoelastic graphene-polymer nanocomposites, *Science* 354 (6317) (2016) 1257–1260.
- [44] V. Eswaraiyah, K. Balasubramaniam, S. Ramaprabhu, Functionalized graphene reinforced thermoplastic nanocomposites as strain sensors in structural health monitoring, *J. Mater. Chem.* 21 (2011) 12626–12628.
- [45] H. Liu, Y. Li, K. Dai, G. Zheng, C. Liu, C. Shen, X. Yan, J. Guo, Z. Guo, Electrically conductive thermoplastic elastomer nanocomposites at ultralow graphene loading levels for strain sensor applications, *J. Mater. Chem. C* 4 (2016) 157–166.